Materials Today Bio 32 (2025) 101714

Contents lists available at ScienceDirect

Materials Today Bio

journal homepage: www.journals.elsevier.com/materials-today-bio

Astragalin-functionalized ultrasmall nanoparticles modulate the complement pathway to inhibit microglial synaptic phagocytosis for reducing anesthetic neurotoxicity

Gang Wang [a,b,c,1], Yaobao Han [c,1], Ke Peng [a,b], Zhilin Jiang [c], Tingting Wang [c], Qing Zheng [c], Wenting Li [a,b,c], Hanbing Xu [a,b,c], Fuhai Ji [a,b,*], Zhen Li [c,**]

[a] Department of Anesthesiology, The First Affiliated Hospital of Soochow University, Suzhou, Jiangsu, China
[b] Institute of Anesthesiology, Soochow University, Suzhou, Jiangsu, China
[c] Center for Molecular Imaging and Nuclear Medicine, State Key Laboratory of Radiation Medicine and Protection, School for Radiological and Interdisciplinary Sciences (RAD-X), Suzhou Medical College, Soochow University, Collaborative Innovation Center of Radiation Medicine of Jiangsu Higher Education Institutions, Suzhou, 215123, China

ARTICLE INFO

Keywords:
Biomimetic nanoparticles
sevoflurane-induced neurotoxicity
Complement
Microglial phagocytosis
Synapse elimination

ABSTRACT

Synaptic impairment is identified as a primary pathology in sevoflurane-induced neurotoxicity, contributing to neurobehavioral and neurodevelopmental deficits. Synaptic loss in neurons occurs through microglia-mediated synaptic phagocytosis *via* the complement pathway. Astragalin, a natural flavonoid compound, exhibits diverse bioactivities, such as anti-tumor, anti-complement, and anti-inflammatory effects. Herein, astragalin-functionalized $Cu_{2-x}Se$ nanoparticles (CSPA NPs) can effectively inhibit the complement pathway, mitigating microglia-mediated synaptic phagocytosis and promoting synaptic restoration to repair sevoflurane-induced neurotoxicity. They efficiently target and reduce microglial activation and phagocytosis. By downregulating sortilin, CSPA NPs increase progranulin expression, promoting TFEB cytoplasmic translocation to decrease lysosomal activity and microglial phagocytosis. Furthermore, CSPA NPs decrease complement C1q and C3 levels, inhibiting microglial synaptic engulfment and ameliorating cognition dysfunction in sevoflurane-treated mice. This study illustrates that CSPA NPs inhibit microglial synaptic elimination *via* the complement pathway, alleviating sevoflurane-induced neurotoxicity and providing insights into treating complement pathway-related diseases.

1. Introduction

Anesthesia induced neurotoxicity in developing brains has raised concerns about potential learning and behavioral impairments in later childhood [1–4]. Recent studies have suggested that anesthetics exposure during the fetal or neonatal stage may lead to neurodevelopmental challenges, including reduced motor skills, poor academic achievement, and language impairments [5,6]. Sevoflurane, commonly used for pediatric anesthesia, offers shorter induction and recovery phases than other agents and is known to cause developmental neurotoxicity. The associated mechanisms include neuroinflammation, neuronal cell damage and apoptosis, demyelination, and microglia activation, contributing collectively to cognitive dysfunction [7–10]. The neurotoxic effects of sevoflurane are associated with damage to hippocampal synapses [11], evident through loss of synapses, decreased synaptic transmission, and m6A modifications in synaptic genes [12–14,65]. Therefore, it is of great importance to eliminate the neurotoxic effects of sevoflurane on the developing brain, which has not been well investigated and solved.

Microglia, the resident immune cells in the brain, are significantly involved in the neurotoxicity caused by sevoflurane [15–17]. Activation of microglia by sevoflurane leads to their transformation into proinflammatory M1-type microglia, intensifying neurodevelopmental disturbances [18,19]. Additionally, microglia are integral to synaptic

* Corresponding author. Department of Anesthesiology, The First Affiliated Hospital of Soochow University, Suzhou, Jiangsu, China.
** Corresponding author.
E-mail addresses: jifuhai@suda.edu.cn (F. Ji), zhenli@suda.edu.cn (Z. Li).
[1] These authors contribute equally.

https://doi.org/10.1016/j.mtbio.2025.101714
Received 4 October 2024; Received in revised form 10 March 2025; Accepted 28 March 2025
Available online 28 March 2025

pruning, actively clearing excessive synapses, cellular debris, and dying cells through phagocytosis [20]. In newborns, neurons initially form numerous synapses, which are later pruned by microglia [21]. This process also plays a role in synaptic loss observed in neurodegenerative conditions like Alzheimer's disease (AD) and Huntington's disease (HD) [22,23].

Microglial phagocytosis of synapses relies on the complement system, which is a part of adaptive innate immunity [24]. A recent study reported that C1q, a key initiator of the classical complement cascade, together with C3, facilitates synaptic refinement during neurodevelopment [25]. When bound to synapses, C1q initiates the complement cascade, leading to C3 cleavage into C3b. Microglia then engulf C3b-marked synapses *via* their CR3 receptors. Overactivation of the complement system can obstruct proper neural connections [26], thereby contributing to various neurodegenerative disorders, including demyelinating diseases, AD, and frontotemporal dementia (FTD) [27–29]. Thus, inhibiting the complement pathway is crucial for preventing and treating neurodegenerative diseases [22,30].

Several potential anti-complement therapeutic strategies exist, such as blocking C1q activation, disrupting convertase assembly, and inhibiting the cleavage of C5 [31,32], with the latter showing notable efficacy. However, the high costs of these treatments restrict their widespread clinical application. Moreover, delivering these therapeutic agents effectively to lesion area is very challenging due to the blood-brain barrier (BBB) [33]. Developing innovative agents with capability of crossing the BBB and exhibiting anti-complement activity is, therefore, essential.

In another study, we reported that quercetin functionalized Cu_{2-x}Se-PVP nanoparticles (CSP NPs), exhibiting multiple enzymatic activities, can induce microglia toward the anti-inflammatory M2 phenotype, thus mitigating neuroinflammation [34]. These nanoparticles, when coated with the cell membrane and aided by ultrasound, can target microglia and cross the BBB [35,36]. They also aid in removing α-syn aggregates from neurons and improving mitochondrial function, offering potential benefits for treating Parkinson's disease (PD) [37–39].

This study presents findings that conjugates of astragalin and ultrasmall Cu_{2-x}Se-PVP (CSPA NPs) can effectively mitigate sevoflurane-induced neurotoxicity in mice (Scheme 1). Mechanistically, CSPA NPs increase PGRN expression and prevent TFEB nuclear translocation, substantially reducing microglial activation and phagocytosis through the lysosome. By inhibiting the complement pathway and microglial synaptic phagocytosis, CSPA NPs alleviate synaptic damage and cognitive deficits associated with sevoflurane. This study demonstrates the importance of suppressing the complement pathway by advanced nanotherapeutics in alleviating the anesthetics-induced neurotoxicity.

2. Results and discussion

2.1. Microglia was involved in sevoflurane induced neurotoxicity

Accumulating evidence has highlighted the role of microglia in cognition development via phagocytosis [40]. By activating microglia, sevoflurane switched microglia from a resting phenotype towards a phagocytic phenotype [41], indicated by their increased soma size, decreased total branch endpoints and length (Fig. 1a). Additionally, microglia (IBA^+, red) showed more colocalization with CD68 (green, a lysosome marker) (Fig. 1b) and had more lysosomal protein expressions (CTSD and Lamp1) after sevoflurane exposure (Fig. S1a). The double-stained of IBA1 (a microglial marker) and PSD95 (a marker of synapse) revealed more $PSD95^+$ puncta within $IBA1^+$ microglia in sevoflurane-treated mice, demonstrating that activated microglia exhibited stronger phagocytic ability and engulfed more synapses

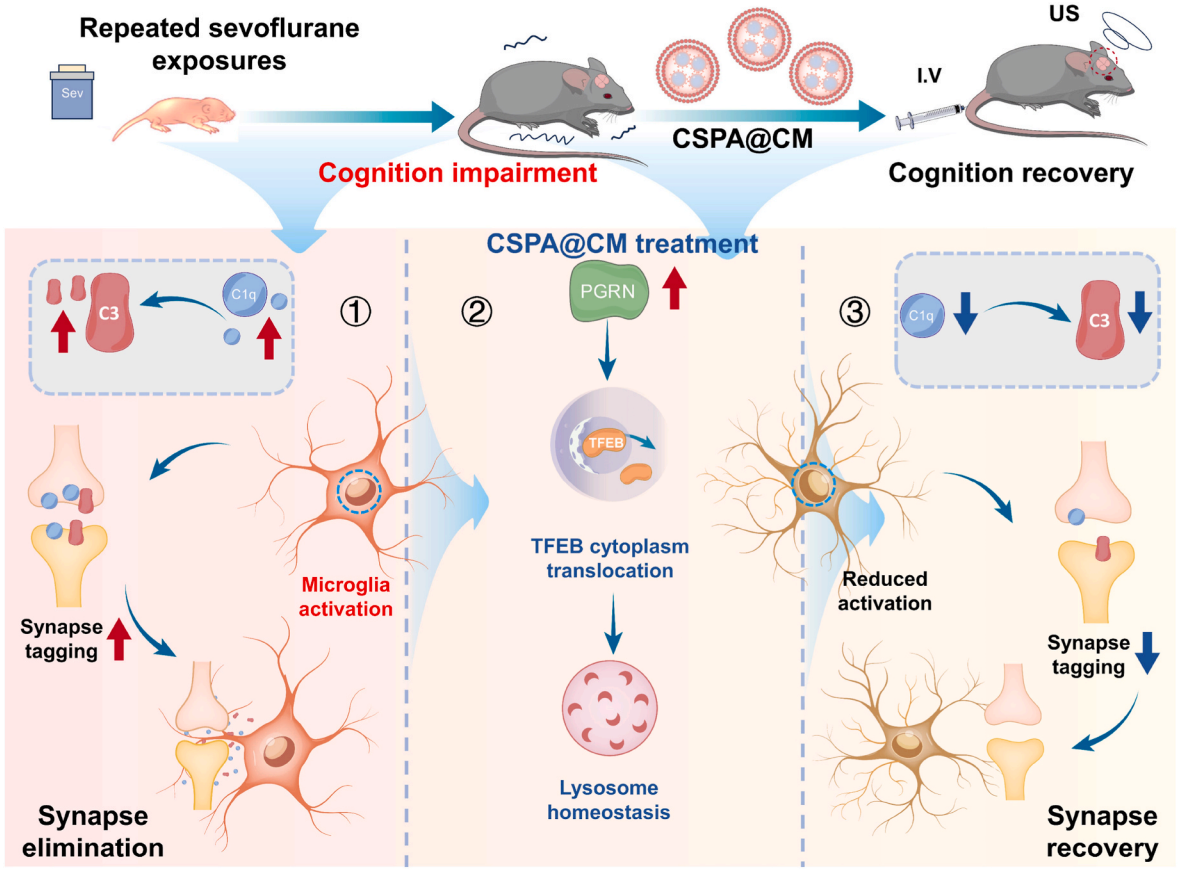

Scheme 1. Schematic illustration of the therapeutic role of multifunctional nanoparticles in sevoflurane-induced neurotoxicity by modulating microglial synaptic elimination and the complement pathway.

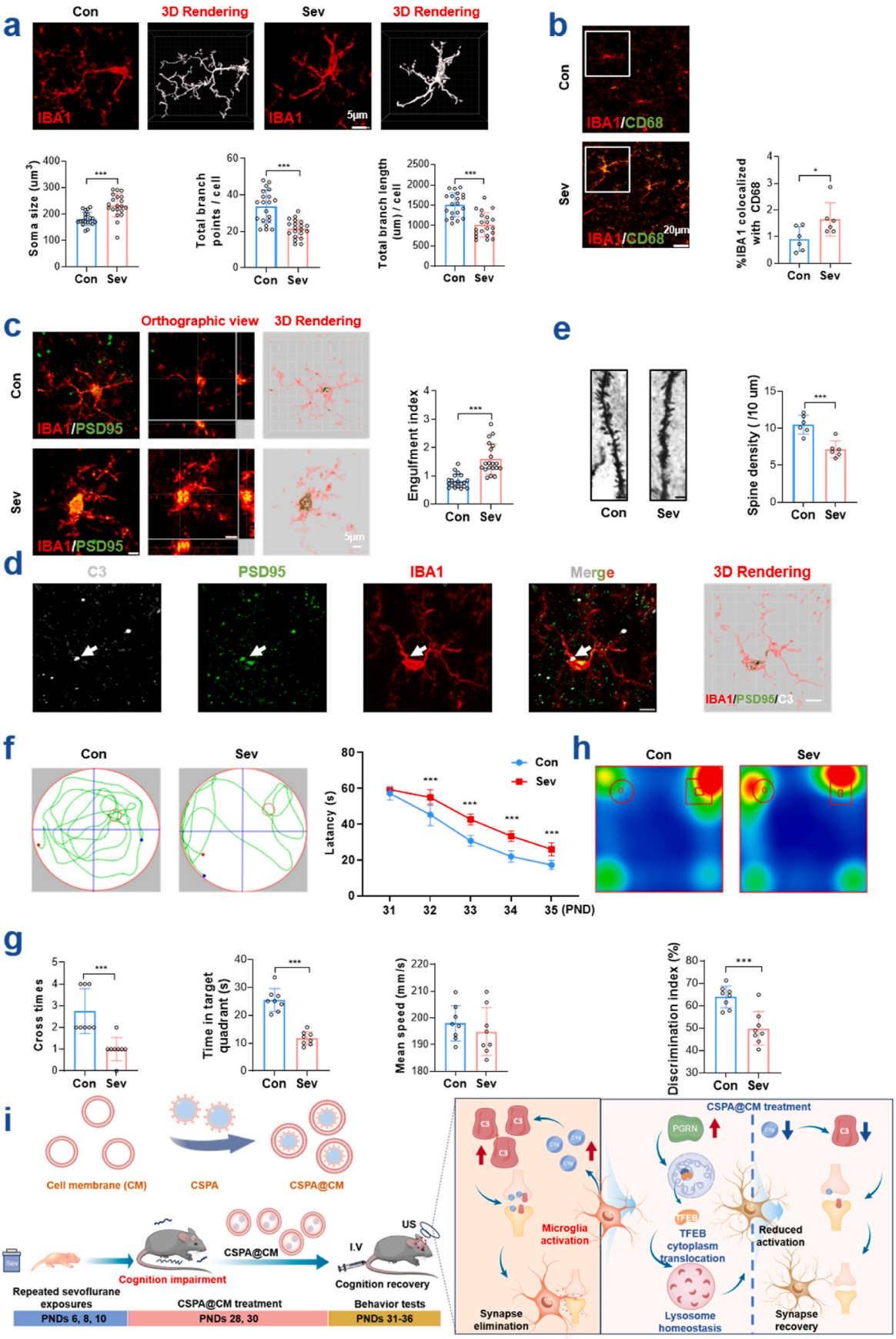

(caption on next page)

Fig. 1. (a) Representative confocal microscopy images and skeleton analysis of microglial morphology in the CA1 region of two groups of mice (scale bar = 5 μm, n = 20). (b) Representative confocal microscopy images and colocalization quantification of CD68 (green) and IBA1 (red) in the CA1 region of two groups of mice (scale bar = 20 μm, n = 6). (c) Representative confocal microscopy images and analysis of $IBA1^+$ microglia (red) containing $PSD95^+$ puncta (green) in the CA1 region of two groups of mice. 3D rendering was shown (scale bar = 5 μm, n = 20). (d) Representative confocal microscopy images of C3 (grey)-labeled PSD95 (green) within microglia (red) in the CA1 region (scale bar = 5 μm). (e) Representative Golgi-Cox staining images and quantification of dendritic spines in the hippocampus of mice (scale bar = 5 μm, n = 6). (f) The tracking paths and escape latency of the mice in the MWM test (n = 8). (g) The platform crossing times, time spent in the target quadrant and swimming speed of the mice in the MWM test (n = 8). (h) Representative motion track and analysis of mice in the NOR test (n = 8). (i) Schematic illustration of targeting microglia and complement cascade to boost the therapeutic of sevoflurane-induced neurotoxicity by CSPA NP. An unpaired *t*-test was used for comparisons between the two groups. Two-way ANOVA followed by a Tukey's post-hoc test was used for multiple comparisons. The data were presented as the mean ± SEM. $^*P < 0.05$, $^{**}P < 0.01$, $^{***}P < 0.001$.

(Fig. 1c). The classical complement cascade has been reported related to microglial engulfment. By tagging synapses, C1q activates the complement pathway and promotes the binding of synapses by C3 for microglial phagocytosis via CR3 receptors [42–44]. We found that after sevoflurane treatment, the expressions of C1q and C3 were elevated (Figs. S1b and c), and colocalization analysis of PSD95 with C1q or C3 showed a notable increase in complement-tagged synapses in sevoflurane-treated mice (Fig. S1d). Staining of C3, PSD95, and IBA1 revealed that the C3-tagged $PSD95^+$ synapses were engulfed by $IBA1^+$ microglia in the CA1 region (Fig. 1d). Microglial synaptic phagocytosis resulted in a robust reduction in synaptic protein expression and dendrite spines density (Fig. 1e–S1e, f). Meanwhile, mice in the sevoflurane group showed cognition dysfunction, evidenced by their prolonged escape latency and fewer platform crossings in the MWM test and lower discrimination index in the NOR test (Fig. 1f–h). These findings indicate that repeated neonatal exposure to sevoflurane induces learning and memory impairment *via* complement-mediated synapse loss. Therefore, suppressing the expression of complement cascade and microglial phagocytosis is promising for enhancing the therapeutic efficacy against sevoflurane-induced neurotoxicity (Fig. 1i).

2.2. Design and characterization of CSPA nanoparticles

Previous findings confirmed that polyvinylpyrrolidone-modified ultrasmall CSP NPs can be efficiently delivered into the brain with ultrasound assistance [35]. Astragalin (As), a flavonoid known for its significant anticomplement activity *in vitro* [45], can decrease the production of NO, iNOS, and proinflammatory cytokines in microglia, and promote the polarization of microglia toward the M2 phenotype [46,47]. Consequently, CSP NPs were selected and modified with astragalin to impede the complement cascade. The resulting conjugates (CSPA NPs, Fig. 2a) are expected to be potent inhibitors for treating complement-mediated diseases, although they have not yet been investigated.

The particle size of CSPA NPs was approximately 2.7 ± 0.06 nm (Fig. 2b and c), as determined by transmission electron microscopy (TEM). The UV–vis spectrum of the CSPA NPs revealed a new absorption peak at 206 nm (Fig. S2a). The hydrodynamic size and Zeta potential of the CSPA NPs were found to be 18.2 nm and −2 mV, respectively (Figs. S2b and c). Using the Fourier transform infrared spectroscopy (FTIR) we also verified the successful conjunction of CSP NPs with astragalin (Fig. S2d). The weight ratio of astragalin in the CSPA NPs was estimated to be about 5 % via thermogravimetric analysis (TGA) (Fig. S2e). These characterizations confirmed the effective functionalization of CSP NPs with astragalin.

2.3. CSPA NPs reduced microglial activation and phagocytosis by regulating lysosomal function

As mentioned previously, microglia play important roles in the phagocytosis of synapses, clearance of apoptotic cells, immune surveillance, and pathogen defense during brain development [48]. Our previous study demonstrated that sevoflurane promoted microglia activation and enhanced their phagocytic property. The influence of CSPA NPs on microglial activation and phagocytosis was thus investigated (Fig. 2d) by co-expressing BV2 cells with CD68 (green) and IBA1 (red). After incubation with sevoflurane for 6 h, BV2 cells were treated with 0.06, 0.125, or 0.25 mM CSPA NPs (determined by the CCK-8 assay) (Fig. S3) for 12 h. Immunofluorescence results showed a significant increase in CD68 and IBA1 expression due to sevoflurane, which was markedly reduced after treatment with 0.25 mM CSPA NPs (Fig. 2e and f). CSPA NPs also decreased the expression of CD11b, a marker of microglial phagocytosis, in sevoflurane-treated BV2 cells (Figs. S4a and b). Additionally, the expression of microglial phagocytic genes, such as TLR 2, TLR 7, TLR 13, ITAM, and CXCR4, was suppressed by CSPA NPs in BV2 cells, compared to their expression in cells treated with sevoflurane (Fig. 2g) [49]. These findings indicate that CSPA NPs can effectively inhibit microglial activation and phagocytosis.

To further elucidate the effects of CSPA NPs on microglia, we investigated their impact on lysosomes, which play a crucial role in degrading debris, synapses, and pathogens engulfed by microglia [50]. The phagocytosis of microglia requires optimal lysosomal acidity and functions to complete the degradation and recycling of endocytosed materials [51,52]. To evaluate whether the reduction in microglial phagocytic function induced by CSPA NPs was associated with a decrease in lysosomal activity, lysosomes were labeled with LysoTracker Green (Fig. 2h) and varying lysosome sizes were observed in different cell groups. Compared to no treatment, sevoflurane treatment significantly increased lysosomal size, whereas CSPA NPs (0.25 mM) suppressed this enlargement. Lysosomal pH changes were determined using LysoSensor (Figs. S5a and b), which emits blue fluorescence (Ex/Em = 329 nm/440 nm) in a neutral environment and yellow fluorescence (Ex/Em = 384 nm/540 nm) in more acidic conditions. The lysosomal pH in BV2 cells treated with sevoflurane decreased, as indicated by strong yellow fluorescence, whereas it increased in cells treated with CSPA NPs, as determined by intense blue fluorescence (Figs. S5a and b).

To better elucidate the effects of CSPA NPs on microglial lysosomal function, we analyzed the activity of lysosomes containing lysosome-associated membrane protein 1/2 (Lamp1/2), and the lysosomal hydrolytic enzymes cathepsin B and D (CTSB and CTSD). Western blotting analysis showed that compared to no treatment, sevoflurane significantly upregulated the expression of Lamp1/2, CTSB, and CTSD. In contrast, CSPA NPs (0.25 mM) significantly downregulated the expression of these proteins, thus reducing lysosomal activity (Fig. 2i and j). These findings suggest that CSPA NPs can effectively decrease the activation and phagocytic ability of microglia by influencing their lysosomal function and activity.

2.4. CSPA NPs restored microglial lysosomal homeostasis

Lysosomes are responsible for degrading macromolecules obtained from the extracellular space through endocytosis or phagocytosis. The function of lysosomes is closely related to that of progranulin (PGRN), which is essential for regulating microglial lysosome formation and function [53]. Mice deficient in PGRN show increased expression of lysosomal membrane proteins and hydrolases, such as CD68, Lamp1, and CTSD, which promote lysosomal biogenesis [54]. Moreover, the absence of PGRN can result in an abnormal increase in microglial phagocytosis and enhanced microglia-mediated synapse engulfment through the complement pathway [29,55,56]. Thus, we investigated the

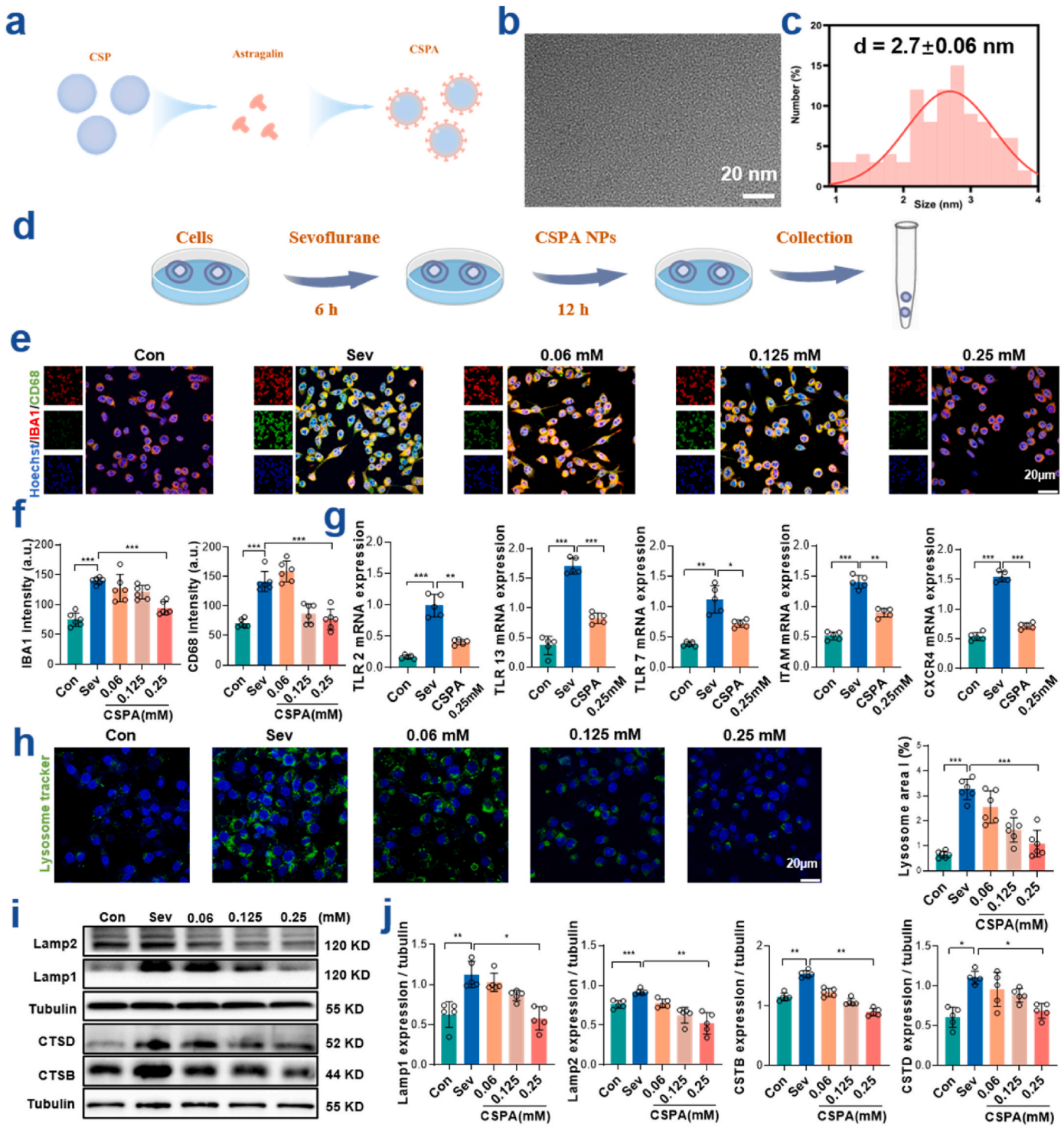

Fig. 2. (a) Schematic illustration of the synthesis of CSPA NPs. (b, c) TEM image and particle size distribution of CSPA NPs. (d) Schematic illustration of sevoflurane exposure and CSPA NPs treatment in BV2 microglial cells. (e) Representative confocal microscopy images of IBA1 (red) and CD68 (green) in BV2 cells treated with different concentrations of CSPA NPs for 12 h after sevoflurane exposure (scale bar = 20 μm). (f) Immunofluorescence analysis of IBA1 and CD68 expression in BV2 cells treated with different concentrations of CSPA NPs for 12 h after sevoflurane exposure (n = 6). (g) The expressions of the microglial phagocytosis-related genes, TLR2, TLR7, TLR13, ITAM, and CXCR4 in BV2 cells treated with different concentrations of CSPA NPs for 12 h after sevoflurane exposure were analyzed by q-PCR (n = 5). (h) Representative confocal microscopy images and analysis of lysosomes in BV2 cells treated with different concentrations of CSPA NPs for 12 h after sevoflurane exposure (scale bar = 20 μm). (i, j) Western blot and quantification of lysosomal protein expressions in BV2 cells treated with different concentrations of CSPA NPs for 12 h after sevoflurane exposure (n = 5). Two-way ANOVA followed by a Tukey's post-hoc test was used for comparisons among multiple groups. The data were presented as the mean ± SEM. *$P < 0.05$, **$P < 0.01$, ***$P < 0.001$.

effect of CSPA NPs on PGRN expression. Immunofluorescence showed that PGRN intensity was lower in the sevoflurane treatment group than in the control group, and significantly higher in the CSPA NP (0.25 mM) group (Fig. 3a and b). Additionally, Western blotting analysis confirmed that CSPA NPs upregulated PGRN levels in sevoflurane-treated BV2 cells (Fig. 3c–e), similar to the effect of the PGRN agonist chloroquine (Chq, 50 μM) (Fig. 3d–f). The regulation of lysosomal function by PGRN depends on the transcription factor EB (TFEB), a critical transcription factor involved in lysosomal formation and autophagy [57]. The nuclear translocation of TFEB can increase both the number of lysosomes and the levels of lysosomal enzymes, thus enhancing phagocytic and degradation activity [58]. By inhibiting the nuclear translocation of TFEB, PGRN can maintain lysosomal homeostasis and reduce phagocytosis in microglia [59]. We stained TFEB in BV2 cells to investigate its nuclear translocation induced by CSPA NPs. Immunofluorescence analysis revealed that TEFB was mainly expressed in the cytoplasm of BV2 cells without sevoflurane exposure, *i.e.*, under normal culture conditions (Fig. 3g). Treatment with sevoflurane resulted in TFEB nuclear translocation to promote lysosomal biogenesis, while CSPA NPs (0.25 mM) significantly inhibited this translocation (Fig. 3g). Additionally, treatment of BV2 cells with Chq inhibited sevoflurane-induced TFEB nuclear translocation, confirming the dependence of PGRN on TFEB (Fig. S6).

The transport of PGRN is negatively regulated by sortilin, which modulates PGRN signaling [60]. The effect of CSPA NPs on sortilin levels was assessed. The results indicated that sortilin levels were significantly higher in sevoflurane-treated BV2 cells than in untreated cells, whereas CSPA NPs (0.25 mM) suppressed the increase in sortilin levels induced by sevoflurane (Fig. 3h and i). These findings were consistent with the results of Western blotting analysis (Fig. 3j and k). Collectively, these results suggested that CSPA NPs decreased sortilin levels and increased PGRN expression, promoting TFEB cytoplasmic translocation to restore lysosomal homeostasis (Fig. 3l).

2.5. CSPA NPs inhibited C1q/C3 to reduce microglial synaptic phagocytosis

The above-mentioned results highlighted the critical role of the complement pathway in microglia-mediated synapse loss in sevoflurane-treated mice. Inhibiting this pathway is crucial for alleviating synapse impairment. The effects of CSPA NPs on complement components C1q and C3 in BV2 cells were investigated. As observed in mice, sevoflurane increased C1q and C3 expression in BV2 cells. Following sevoflurane exposure, BV2 cells were treated with CSPA NPs. Immunofluorescence and Western blotting results demonstrated that CSPA NPs reduced the expression of C1q and C3 (Fig. 4a–f). These effects occurred due to the synergistic action of CSP NPs and astragalin (Fig. 4g and h). The inhibitory effect of CSPA NPs was similar to that of the C1q-antibody ANX005 (0.1 mM) (Fig. 4i and j).

To determine the potential of CSPA NPs to mitigate microglial-mediated synapse elimination *in vitro* [61], BV2 cells were cultured with fluorescent beads to assess phagocytosis. The results indicated that sevoflurane-treated BV2 cells phagocytosed significantly more beads than untreated cells, while CSPA NPs decreased phagocytosis, as determined by fewer endocytosed beads in the cells (Fig. 4k, Fig. S7a). To simulate the effect of microglia on synapses after exposure to sevoflurane, we directly cocultured BV2 and HT22 cells as previously reported [62]. Immunofluorescence images demonstrated that more NeuN (a synaptic marker)-labeled HT22 cells were co-localized with IBA1 (a microglial marker)-labeled BV2 cells in the sevoflurane group, indicating that sevoflurane promoted synapse elimination by microglia. Moreover, treatment with CSPA NPs after exposure to sevoflurane significantly reduced the number of NeuN-positive HT22 and IBA1-positive BV2 cells (Fig. 4l). The bright field images also confirmed that treatment with CSPA NPs reduced the phagocytosis of HT22 cells (ramified) by BV2 cells (round) (Fig. S7b). These findings indicated that CSPA NPs effectively inhibit complement pathway-mediated microglial synaptic phagocytosis *in vitro*.

2.6. Therapeutic efficacy of CSPA NPs on sevoflurane-treated mice

Based on the *in vitro* results, CSPA NPs were applied *in vivo* to reduce complement-mediated microglial elimination of synapses and alleviate sevoflurane-induced cognitive dysfunction in mice. To effectively target microglia, neuronal membranes were used to wrap CSPA NPs, forming CSPA@CM NPs (Fig. S8a), and their targeting capability was enhanced by using specific interactions between integrin alpha 4 and beta 1 (α4β1) on the membrane of microglia [34]. Mice treated with sevoflurane were intravenously injected with CSPA@CM NPs (5 mg/kg) on PNDs 28 and 30. Hematoxylin and eosin (H&E) staining indicated that CSPA@CM NPs did not exert significant toxic effects on the main organs (*i.e.*, the heart, liver, spleen, lung, or kidney) of the mice (Fig. S8b). Copper staining demonstrated effective delivery of CSPA@CM NPs to the hippocampus with the assistance of focused ultrasound, temporarily opening the BBB (Fig. S9).

The mice were divided into five groups to investigate therapeutic efficacy: 1) healthy mice (control group), and sevoflurane-treated mice which were 2) received PBS (Sev + PBS group); 3) received PBS after sonication with focused ultrasound (Sev + PBS + US group); 4) received CSPA@CM NPs (Sev + CSPA@CM group) and 5) received CSPA@CM NPs after sonication with focused ultrasound (Sev + CSPA@CM + US group).

The athletic and cognitive performance of mice in these groups was shown in Fig. 5a. Representative swimming paths in the MWM test were displayed in Fig. 5b. The time finding the platform in the Sev + CSPA@CM + US group was shorter on PNDs 32–33 compared to those in the Sev + PBS group (Fig. 5c). Additionally, treatment of sevoflurane-treated mice with CSPA@CM NPs after FUS (Sev + CSPA@CM + US group) increased the number of platform crossings and the time spent in the target quadrant (Fig. 5d). No significant difference in the mean swimming speed among the five groups was observed, indicating no movement disability (Fig. 5d).

The NOR test indicated a significant increase in the discrimination index following CSPA NP treatment in sevoflurane-treated mice. These results demonstrated that CSPA NPs can effectively alleviate sevoflurane-induced cognition dysfunction (Fig. 5e, Fig. S10). The OFT revealed no differences in the mean speed, total distance traveled, time spent in the central zone, and time required to enter the central zone, indicating that the mice in the five groups did not exhibit anxiety dysfunction (Fig. 5f and g). Additionally, the effects of complement inhibitor RMA combined with CSPA NPs (at the same dose, 5 mg/kg) were investigated, and the NOR and MWM test results demonstrated greater efficacy of CSPA NPs than RMA at the same dosage (Fig. S11).

The effect of CSPA@CM NPs on the activation and phagocytic ability of microglia in sevoflurane-treated mice was evaluated. Morphological analysis showed that compared to the microglia from the Sev + PBS group, the microglia from the Sev + CSPA@CM + US group exhibited a significant reduction in soma size and an increase in branch length (Fig. 6a and b). Moreover, the microglia from the Sev + CSPA@CM + US group showed less co-localization of CD68 with IBA1 (Fig. 6c and d) and more co-localization of IBA1 with PGRN than those from the Sev + PBS group (Fig. S12), indicating that CSPA@CM NPs effectively suppressed the activation and phagocytic capability of microglia by upregulating PGRN.

To further reveal the therapeutic mechanism, we assessed the effects of CSPA NPs on complement cascade in mice. The immunofluorescence (Fig. 6e–h) and Western blotting results (Fig. 6i and j) showed significantly downregulated expression of complement C1q and C3 in microglia from the Sev + CSPA@CM + US group compared to those from the Sev + PBS group. Compared to treatment with Sev + PBS, treatment with CSPA@CM NPs and focused ultrasound significantly decreased the number of synapses engulfed by microglia (Fig. 7a and b). Furthermore,

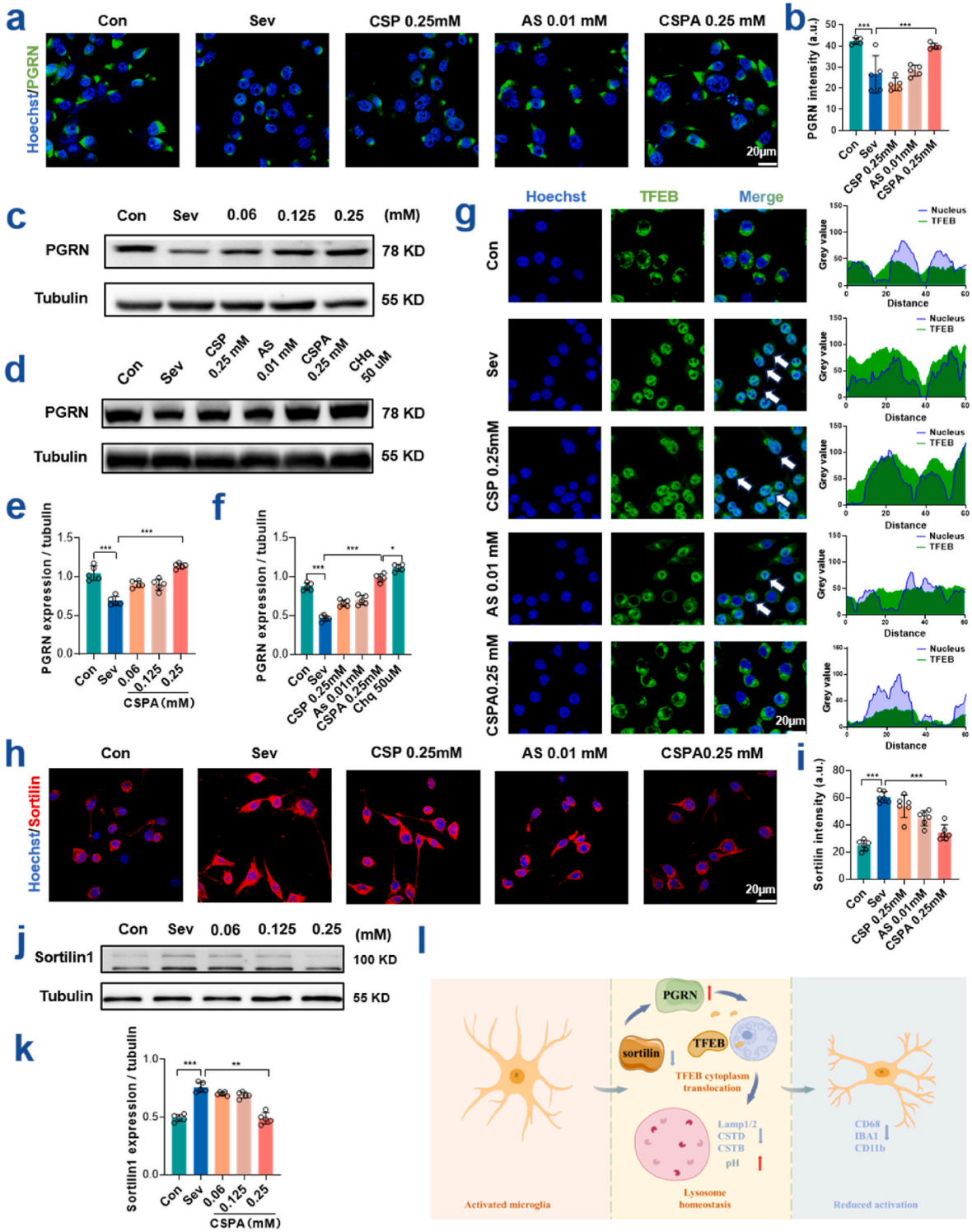

Fig. 3. (a) Representative confocal microscopy images of the expression of PGRN in BV2 cells treated with CSP (0.25 mM), AS (0.01 mM), or CSPA NPs (0.25 mM) for 12 h after sevoflurane exposure (scale bar = 20 μm). (b) Quantification of PGRN expression in BV2 cells treated with CSP (0.25 mM), AS (0.01 mM), or CSPA NPs (0.25 mM) for 12 h after sevoflurane exposure (n = 6). (c, e) Western blot analysis of PGRN level in BV2 cells treated with different concentrations of CSPA NPs for 12 h after sevoflurane exposure (n = 5). (d, f) Western blot analysis of PGRN level in BV2 cells treated with CSP (0.25 mM), AS (0.01 mM), CSPA NPs (0.25 mM), or CHq (50 μM) for 12 h after sevoflurane exposure (n = 5). (g) Representative confocal microscopy images of TFEB nuclear translocation in BV2 cells treated with CSP (0.25 mM), AS (0.01 mM), or CSPA NPs (0.25 mM) for 12 h after sevoflurane exposure (scale bar = 20 μm). (h) Representative confocal microscopy images and (i) analysis of Sortilin expression in BV2 cells treated with CSP (0.25 mM), AS (0.01 mM), or CSPA NPs (0.25 mM) for 12 h after sevoflurane exposure (scale bar = 20 μm, n = 6). (j, k) Western blot analysis of Sortilin expression in BV2 cells treated with different concentrations of CSPA NPs for 12 h after sevoflurane exposure (n = 5). (l) Schematic illustration of the mechanism of CSPA NPs ameliorating lysosomal dysfunction of BV2 cells caused by sevoflurane. Two-way ANOVA followed by a Tukey's post-hoc test was used for comparisons among multiple groups. The data were presented as the mean ± SEM. *$P < 0.05$, **$P < 0.01$, ***$P < 0.001$.

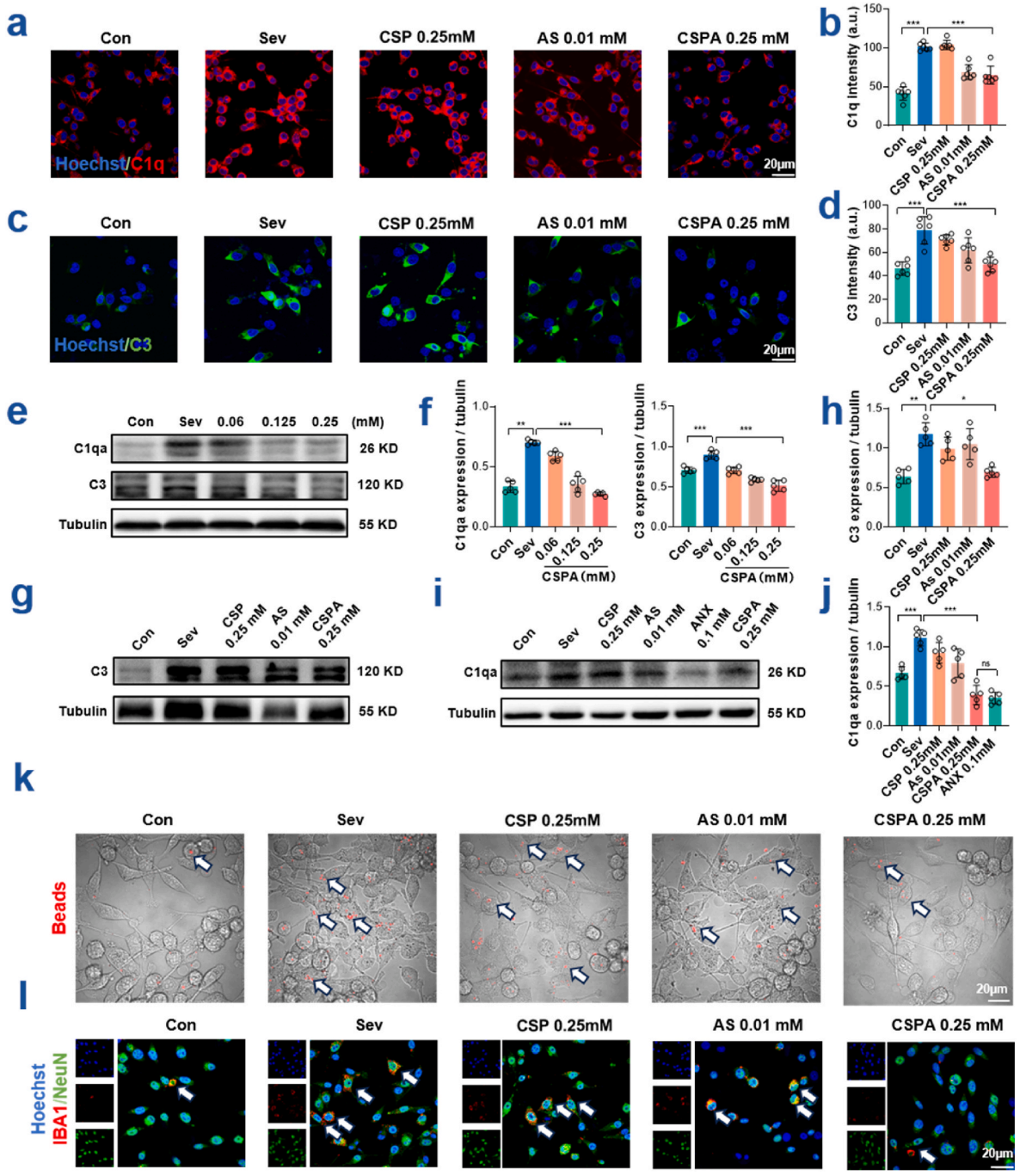

Fig. 4. (a) Representative confocal microscopy images of C1q in BV2 cells treated with CSP (0.25 mM), AS (0.01 mM), or CSPA NPs (0.25 mM) for 12 h after sevoflurane exposure (scale bar = 20 μm). (b) Immunofluorescence analysis of C1q expression in BV2 cells treated with CSP (0.25 mM), AS (0.01 mM), or CSPA NPs (0.25 mM) for 12 h after sevoflurane exposure (n = 6). (c) Representative confocal microscopy images showed the C3 expression in BV2 cells treated with CSP (0.25 mM), AS (0.01 mM), or CSPA NPs (0.25 mM) for 12 h after sevoflurane exposure (scale bar = 20 μm). (d) Quantification of C3 expression in BV2 cells treated with CSP (0.25 mM), AS (0.01 mM), or CSPA NPs (0.25 mM) for 12 h after sevoflurane exposure (n = 6). (e, f) Western blot analysis of C1qa and C3 in BV2 cells treated with different concentrations of CSPA NPs for 12 h after sevoflurane exposure (n = 5). (g, h) Western blot analysis of C3 in BV2 cells treated with CSP (0.25 mM), AS (0.01 mM), or CSPA NPs (0.25 mM) for 12 h after sevoflurane exposure (n = 5). (i, j) Western blot analysis of C1qa in BV2 cells treated with CSP (0.25 mM), AS (0.01 mM), ANX (0.1 mM), or CSPA NPs (0.25 mM) for 12 h after sevoflurane exposure (n = 5). (k) Representative confocal microscopy images of fluorescent beads (red) in BV2 cells treated with CSP (0.25 mM), AS (0.01 mM), or CSPA NPs (0.25 mM) for 12 h after sevoflurane exposure. The results showed that CSPA NPs significantly reduced the phagocytosis of fluorescent beads by BV2 cells after sevoflurane exposure (scale bar = 20 μm). (l) Representative confocal microscopy images of BV2 cells ($IBA1^+$, red) cocultured with HT22 cells ($NeuN^+$, green) treated with CSP (0.25 mM), AS (0.01 mM), or CSPA NPs (0.25 mM) for 12 h after sevoflurane exposure. The results showed that CSPA NPs significantly reduced BV2 cells' phagocytosis of synapses after sevoflurane exposure (scale bar = 20 μm). Two-way ANOVA followed by a post hoc Tukey's test was used for comparisons among multiple groups. The data were presented as the mean ± SEM. $^*P < 0.05$, $^{**}P < 0.01$, $^{***}P < 0.001$.

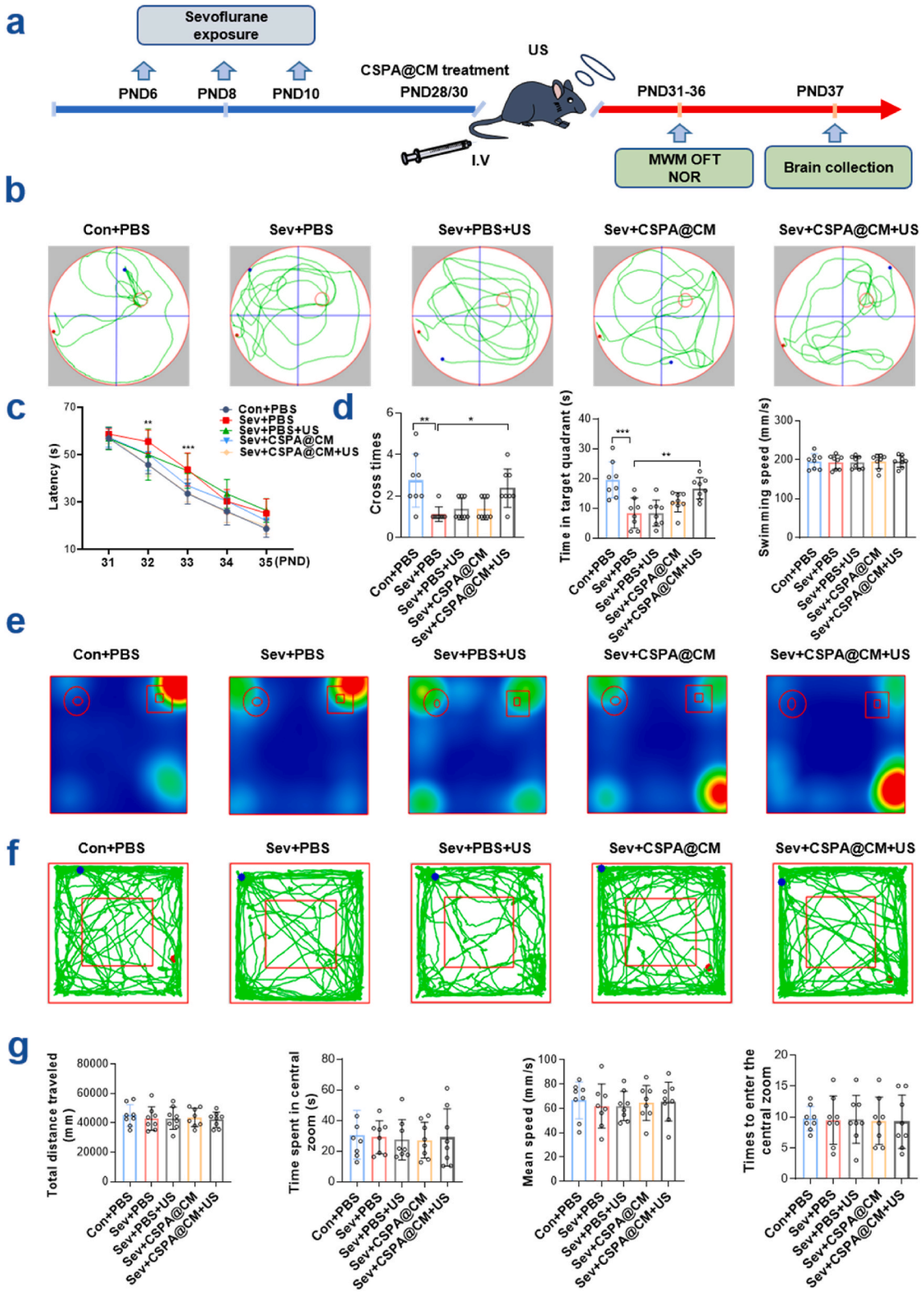

Fig. 5. (a) Schematic illustration of the time course for the treatment and behavioral tests in Con + PBS group, Sev + PBS group, Sev + PBS + US group, Sev + CSPA@CM group, and Sev + CSPA@CM + US group. (b) The MWM test from the five groups of mice. The tracking paths of the mice in the five groups were shown. (c) The escape latency of the mice in the five groups. (d) Analysis of platform crossing times, times spent in the target quadrant, and the swimming speed of the mice in the five groups (n = 8). (e) The NOR test from the five groups of mice. The motion track of the mice in the five groups was shown. (f, g) Open field test. Representative tracking paths and analysis of total distance traveled, time in the central zoom, mean speed, and times to enter the central zoom in the five groups of mice (n = 8). Two-way ANOVA followed by a post hoc Tukey's test was used for comparisons among multiple groups. The data were presented as the mean ± SEM. $^{*}P < 0.05$, $^{**}P < 0.01$, $^{***}P < 0.001$.

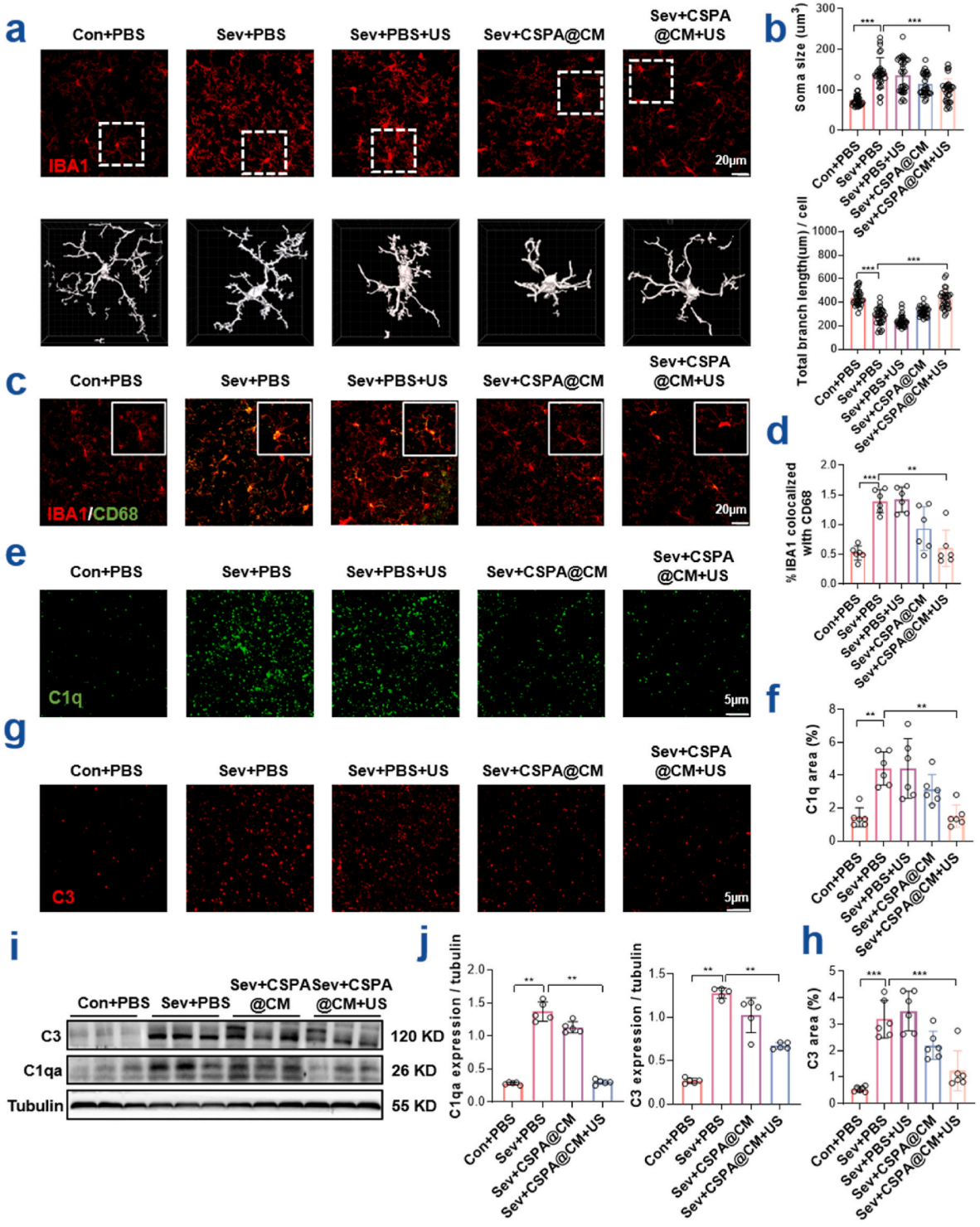

Fig. 6. (a) Representative confocal microscopy images and 3D rendering of IBA1^{+}(red) microglia in the hippocampal CA1 region of mice in the Con + PBS group, Sev + PBS group, Sev + PBS + US group, Sev + CSPA@CM group, and Sev + CSPA@CM + US group (scale bar = 20 μm). (b) Skeleton analysis of microglial morphology in the five groups of mice (n = 20). (c, d) Representative confocal microscopy images and colocalization analysis of IBA1 (red) and CD68 (green) in the CA1 region of mice from the five groups (scale bar = 20 μm, n = 6). (e–h) Representative confocal microscopy images and analysis of the expressions of C1q and C3 in the five groups of mice (scale bar = 5 μm, n = 6). (i, j) Western blot analysis of the expressions of C1qa and C3 in mice from the four groups of mice (n = 5). Two-way ANOVA followed by a post hoc Tukey's test was used for comparisons among multiple groups. The data were presented as the mean ± SEM. $^{*}P < 0.05$, $^{**}P < 0.01$, $^{***}P < 0.001$.

a significant increase in the density of PSD95, Vglut2, and synapses was recorded in the Sev + CSPA@CM + US group compared to that in the Sev + PBS group (Fig. 7c, d, Fig. S13). The results of Western blotting analysis also confirmed the upregulation of PSD95 and Vglut2 protein levels by CSPA@CM NPs and focused ultrasound (Sev + CSPA@CM + US group) (Fig. 7e and f). Golgi staining revealed an increase in dendritic spine density in neurons from the Sev + CSPA@CM + US group of mice (Fig. 7g and h). The electrophysiological results showed that after

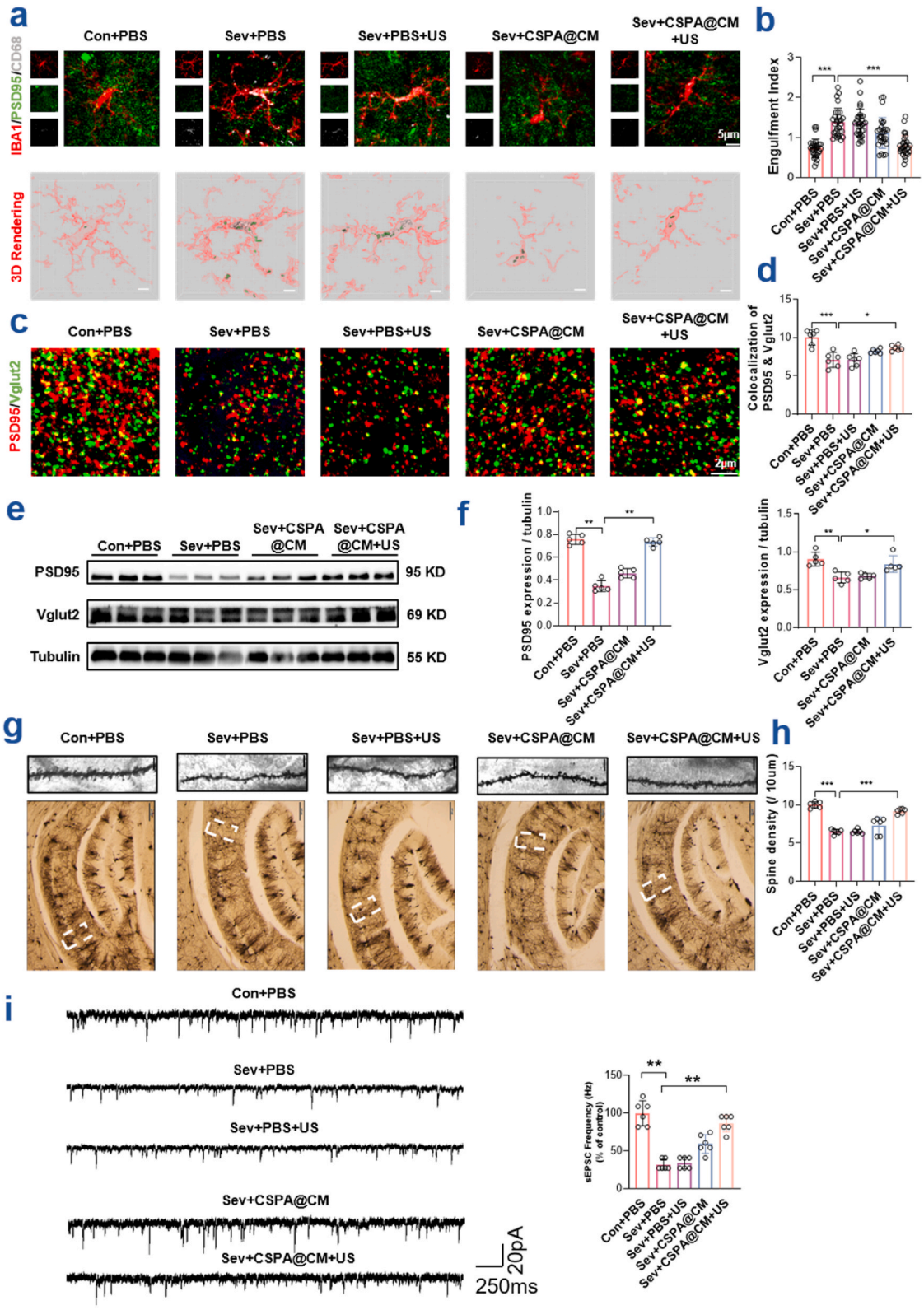

Fig. 7. (a) Representative image of CD68^{+} lysosomes (grey) containing PSD95^{+} puncta (green) in IBA1^{+} microglia (red) in the CA1 region of five groups of mice (scale bar = 5 μm). 3D rendering was shown. (b) Quantification of PSD95^{+} puncta in microglia (IBA1^{+}) in the five groups of mice (n = 20). (c, d) Representative confocal microscopy images and analysis of the colocalization of PSD95 (red) and Vglut2 (green) in the CA1 region of five groups of mice (scale bar = 2 μm, n = 6). (e, f) Western blot analysis of the expression of PSD95 and Vglut2 in the four groups of mice (n = 5). (g, h) Representative Golgi-Cox staining images and quantification analysis of dendritic spine density in the five groups of mice (scale bar = 5 μm, n = 6). (i) Effects of CSPA NPs on spontaneous EPSCs (sEPSCs) in CA1 neurons in the five groups of mice (n = 6). Two-way ANOVA followed by a post hoc Tukey's test was used for comparisons among multiple groups. The data were presented as the mean ± SEM. *$P < 0.05$, **$P < 0.01$, ***$P < 0.001$.

sevoflurane exposure, the frequency of sEPSC was significantly lower. However, after treatment with CSPA NPs, the sEPSC frequency of mice from the CSPA@CM + US group was increased. The result supports that CSPA NPs can improve synaptic restoration and neural plasticity (Fig. 7i).

3. Conclusion

To summarize, our study found that repeated exposure to sevoflurane in neonatal mice can induce developmental neurotoxicity through activation of microglia and enhanced synaptic phagocytosis mediated by the complement cascade. We observed that CSPA NPs effectively decreased microglial activation and phagocytic activity by inhibiting lysosomal function. Specifically, they increased PGRN expression to prevent TFEB nuclear translocation and restore lysosomal balance. By targeting hippocampal microglia, CSPA NPs mitigated the complement cascade and microglial synaptic phagocytosis, thereby reducing synaptic loss and cognitive impairment caused by sevoflurane exposure. In contrast to conventional complement cascade inhibition using antibodies, our study provided a novel approach to suppress complement-mediated microglial synaptic phagocytosis, offering promising therapeutic potential for mitigating sevoflurane-induced neurodevelopmental toxicity and other neurological disorders.

4. Methods

4.1. Synthesis of $Cu_{2-x}Se$ -PVP -astragalin nanoparticles (abbreviated as CSPA NPs)

CSP nanoparticles were synthesized and purified as previously reported [34]. Then 2 mL of CSP solution (1 mg/mL) was diluted with dimethyl sulfoxide (DMSO, V: V = 1:1), and 2 mg of astragalin (As) was dissolved in DMSO. These two solutions were mixed, stirred vigorously for 4 h at room temperature, and dialyzed for another 6 h. Afterward, the solution was centrifuged, and the supernatant was filtered through a 30 kDa membrane to obtain the CSPA NPs solution, which was collected and stored for further use.

4.2. Synthesis of CSPA@CM NPs

MES23.5 cells were suspended in a cold Tris buffer solution (pH = 7.4, containing 1 × ethylenediamine tetra-acetic acid-free protease inhibitor) for 1 h at 4 °C and sonicated (Ultrasonic Cell Disruption System). The resultant supernatants were further centrifuged to obtain the cell membrane debris. Finally, the deposits were suspended in the CSPA solution and extruded through 400 nm membrane to obtain the CSPA@CM NPs.

4.3. Animals

The animal experiments were conducted following ethical guidelines and approved by the Institutional Animal Care and Use Committee of Soochow University (Approval No. 202210A0169). C57BL/6J mice weighing 22–24 g were purchased from the GemPharmatech (Jiangsu China) and maintained on standard diets under a controlled environment (12 h light-dark cycle at 20–22 °C, and relative humidity at 60 %). Male offspring mice were used in the experiments. All procedures complied with the Guide for the Care and Use of Laboratory Animals published by the US National Institutes of Health (NIH Publication No. 85-23, revised in 1996).

4.4. Cell culture and coculture experiments

BV2 cells and HT22 mouse hippocampal neuronal cells were obtained from Fu Heng Biology (Shanghai, China), and Procell Life Science & Technology Co., Ltd. (Wuhan, China), respectively. The cells were maintained in DMEM with 10 % FBS (Gibco, Germany) and 1 % penicillin/streptomycin at 37 °C in a 5 % CO_2 humidified atmosphere.

For the coculture experiment, BV2 cells (5×10^4 cells/well) were seeded in the confocal dishes pre-coated with 10 mg/mL polylysine diluted in PBS for 12 h. Then the HT22 cells (2×10^5 cells/well) were added to the dishes and cocultured with BV2 cells in DMEM containing 10 % (v/v) FBS and 1 % (v/v) penicillin/streptomycin for 12 h.

4.5. Animal and cell models induced by sevoflurane exposure

The neonatal mice (PNDs 6, 8, 10) in the sevoflurane group received a mixture of 3 % sevoflurane with oxygen (60 %) for 2 h daily (2 L/min for anesthesia induction, followed by 1 L/min for maintenance). The control group of mice received 60 % oxygen for 2 h. The concentrations of sevoflurane and oxygen were monitored continuously (Vamos; Dräger Medical, Germany), and the mice were kept warm on a plate at 37 ± 1 °C. After exposure, the mice were promptly returned to their home cages and received standard care.

For cell experiments, sevoflurane stock solutions were prepared according to previous studies [63]. BV2 and HT22 cells were seeded in plates and cultured for 24 h. Then the medium was replaced, and the sevoflurane working solution (containing 3 % sevoflurane) was added to the medium and cultured for another 6 h.

4.6. Assays of cell toxicity

Both BV2 and HT22 cells were seeded in 96-well plates at a density of 1×10^4 cells/well, cultured for 24 h, and incubated with different concentrations of CSPA NPs for 12 h. Then, the cells were washed with PBS and cultured with a new medium containing CCK-8 solution (1:100 dilution, Enhanced Cell Counting Kit-8, Cat. no. C0043, Beyontime) for 2 h at 37 °C. We measured the absorbance at 450 nm with a microplate reader (PerkinElmer EnSpire, Singapore). The relative cell viabilities were calculated according to a previously reported formula [38].

4.7. Assessment of lysosomal activity and pH of BV2 cells

To assess the lysosomal activity and pH of BV2 cells, we seeded them in confocal dishes in a density of 4×10^4 cells/well and cultured for 12 h followed by treatment with CSPA NPs for another 12 h. We then stained the cells with LysoTracker Green (DND-26, Yeasen) or LysoSensor (DND-160, Yeasen) for 30 min before fixation with 4 % paraformaldehyde. The nuclei were stained with Hoechst 33342. Images were acquired with a confocal microscope (FV1200, Olympus, Japan) using a 63 × /1.3 NA oil objective.

4.8. In vitro assay of microglial phagocytosis

In the *in vitro* phagocytosis assay, BV2 cells, at a density of 1×10^4 cells per well, were initially seeded in confocal dishes and cultured for 24 h. Following this incubation period, the culture medium was replaced, and the cells were subjected to treatment with a 3 % sevoflurane solution for 6 h. After treatment, the medium was removed, and the cells were washed with PBS before being placed in a fresh medium to continue the experiment. Next, fluorescent latex beads, specifically 1 μm in size (L2778, Sigma), were pre-opsonized using a solution composed of 50 % fetal bovine serum (FBS) mixed with PBS. Once prepared, these beads were added to the cells at a concentration of 50 beads per cell and incubated at 37 °C for an additional 6 h. Following this incubation, the cells underwent gentle washing processes to eliminate any unbounded beads. Subsequently, the cells were fixed using a solution of 4 % paraformaldehyde to preserve their structure for imaging. Finally, images were captured using an Olympus FV1200 confocal microscope (Olympus, Japan), which was equipped with a 63 × /1.3 NA oil immersion objective lens.

4.9. Western blot

The hippocampi of the mice and cells were collected and lysed with radioimmunoprecipitation (RIPA) buffer and phenylmethanesulfonyl fluoride (PMSF) (Beyotime, Shanghai, China) on ice. The protein concentration was determined and quantified by a BCA assay (Beyotime, Jiangsu, China). Then 30 μg of protein was separated by sodium dodecyl sulfate-polyacrylamide gel electrophoresis (SDS-PAGE) gel and transferred to a polyvinylidene fluoride (PVDF) membrane (Millipore, Germany). The membrane was washed with TBST for 10 min three times and blocked with 5 % nonfat milk for 2 h at room temperature. The following primary antibodies were incubated at 4 °C overnight: CTSD (1:1000, 31718, Cell Signaling Technology), CTSB (1:1000, 52899SF, Cell Signaling Technology), Lamp1 (1:1000, 67300-1, Proteintech), Lamp2 (1:1000, 27823-1-AP, Proteintech), PGRN (1:1000, abs137474, Absin), sortilin (1:1000, 12369-1-AP, Proteintech), C1q (1:1000, DF7839, Affinity), C3 (1:1000, 21337-1-AP, Proteintech), PSD95 (1:1000, 381001, Zenbio) and Vglut2 (1:1000, NBP2-59330, NOVUS). The membrane was subsequently washed three times for 5 min each with TBST on the next day, and incubated with HRP-labeled secondary goat anti-mouse (1:2000; Beyotime, A0216) and goat anti-rabbit (1:2000; Beyotime, A0208) antibodies for 2 h at room temperature. Finally, the bands were imaged with a Tanon 5200 (Tanon Science & Technology Co. Ltd) and analyzed with Image J analysis software package (NIH). The protein expressions were normalized to that of β-tubulin.

4.10. q-PCR analysis

To determine the effects of CSPA on the phagocytic capability of BV2 cells, BV2 cells were seeded in a six-well plate at a density of 4×10^4 cells/well and cultured for 12 h. Then they were treated with 3 % sevoflurane solution for 6 h, followed by treatment with CSPA NPs for another 12 h. Total RNA was extracted using Simply P Total RNA Extraction Kit (Cat. no. BSC52S1, Bioer) according to the manufacturer's instructions. Total RNA was reverse-transcribed into cDNA by HiScript II Q RT SuperMix (Cat. no. R223-01, Vazyme Biotech Co., Ltd.). The expressions of the mRNA levels were quantified with a ViiA 7 Real-Time PCR System (ViiA-7, Life Technologies) using SYBR® Green qPCR (Cat. no. Q711-02-03, Vazyme Biotech Co., Ltd). The following primers (Sangon Biotech Inc, China) were used: mouse β-Tubulin (forward, 5′-CAG CGA TGA GCA CGG CAT AGA C-3′; reverse, 5′-CCA GGT TCC AAG TCC ACC AGA ATG-3′); mouse TLR2 (forward, 5′-GAC TCT TCA CTT AAG CGA GTCT-3′; reverse, AAC CTG GCC AAG TTA GTA TCTC-3′); mouse TLR7 (forward, 5′-TGT GAT GCT GTG TGG TTT GTC TGG-3′; reverse, 5′-TTT GAC CTT TGT GTG CTC CTG GAC-3′); mouse TLR13 (forward, 5′-CAG CCA GGC AGC CAG AGT TTAC-3′; reverse, 5′-GTG CTG AGG ACC ATA CTG AAG GAAC-3′); mouse ITAM (forward, 5′-GAG CAT CAA TAG CCA GCC TCA GTG-3′; reverse, 5′-CCA ACA GCC AGG TCC ATC AAGC-3′); and mouse CXCR4 (forward, 5′-CTC ATC CTA GCT TTC TTT GCCT-3′; reverse, 5′-GAA GTC ACA TCC TTG CTT GATG-3′). The expressions of mRNA were normalized to that of β-tubulin.

4.11. Immunohistochemistry

Mice were deeply anesthetized with pentobarbital (50 mg/kg, intraperitoneal injection) and perfused transcardially with PBS and 4 % paraformaldehyde. The brain was removed after being fixed with 4 % paraformaldehyde for 4 h, and subjected to cryoprotection by sequentially immersing it in 10 %, 20 %, and 30 % sucrose at 4 °C for 24 h. Afterward, the brain was embedded in an optimal cutting temperature (OCT) compound and stored at −80 °C. Coronal slices with a thickness of 20 μm were prepared using a Leica cryostat microtome (Leica CM1950). For immunohistochemistry analysis, the slices were washed with PBS for 5 min three times, subsequently blocked with freshly prepared blocking solution (5 % BSA and 0.2 % Triton X in PBS) for 2 h at room temperature, incubated with primary antibody at 4 °C overnight, and washed with PBS for 10 min three times. The primary antibodies used were as follows: PSD95 (1:200, 381001, ZENBIO), PSD95 (1:200, ab12093, Abcam), Vglut2 (1:200, NBP2-59330, NOVUS), C1q (1:200, DF7839, Affinity), C1q (1:200, 67063-1, Proteintech), IBA1 (1:400, ab283342, Abcam), CD68 (1:200, 29176, CST), CD11b (1:200, R380675, ZENBIO), C3 (1:200, 21337-1-AP, Proteintech), C3 (1:200, PA1-29715, Invitrogen), PGRN (1:200, abs137474, Absin), TFEB (1:200, AG3609, Beyontime), sortilin (1:200, 12369-1-AP, Proteintech), and NeuN (1:200, 26975-1-AP, Proteintech). Next, the slices were incubated with the following secondary antibodies for 2 h at room temperature: Alexa Fluor 488-labeled Goat Anti-Rabbit (1/200, A0423, Beyotime), Alexa Fluor 647-labeled Goat Anti-Rabbit (1:200, A0468, Beyotime), Cy3-labeled Goat Anti-Mouse IgG (1:200, A0521, Beyotime), and Alexa Fluor 488-labeled Donkey anti-Goat (1:200, A-11055, Invitrogen). Finally, the brain slices were stained with Hoechst 33342 (1:1000, C1022, Beyotime) for 10 min, followed by three subsequent washes. Images were acquired with an Olympus FV1200 confocal microscope (Olympus, Japan) using a 63 × /1.3 NA oil objective.

4.12. Three-dimensional (3D) reconstruction

Brain slices were imaged with an Olympus FV1200 confocal microscope (Olympus, Japan) using a 63 × /1.3 NA oil objective, and Z stacking was performed with 0.5 μm/step in the z-direction (z = 20–30 frames). Microglia were imaged in the hippocampal CA1 region in 2–3 tissue slices per animal for a total of 3–4 animals per group and images were further analyzed using IMARIS 9.0.1 software (Bitplane, Switzerland).

4.13. In vivo assay of microglial phagocytosis

For the *in vivo* phagocytosis assay, we co-stained the microglial marker IBA1 and the postsynaptic marker PSD95. Three-dimensional image rendering of z-stack images using Imaris is based on the protocol reported by Schafer et al. (2014) [64]. We first created a 3D surface rendering on the IBA1 channel with a threshold established to enable precise reconstruction of microglial processes, which was then used for subsequent reconstructions. Subsequently, the PSD95 channel was masked to the IBA1 surface to obtain only PSD95 within the analyzed cell. The volumes of microglia and PSD95 were calculated, and the engulfment index was calculated as the volume of internalized PSD95/volume of microglia.

4.14. Microglial morphology analysis

Confocal z-stacks were taken with an Olympus FV1200 confocal microscope (Olympus, Japan) using a 63 × /1.3 NA oil objective. The interval of z-steps was set at 0.5 μm and 20–30 frames were acquired for analysis. Z-stack images were converted into single-plane maximal intensity projections and a threshold was applied. Subsequently, the images were processed by binarization and unsharp masking to eliminate noise. After that, they were skeletonized and analyzed using the AnalyzeSkeleton plugin in Image J software.

4.15. Golgi staining

Golgi staining was performed according to the manufacturer's instructions for the FD Rapid Golgi Staining Kit (PK401, FD NeuroTechnologies, United States). The brains of the mice were collected and submerged in a mixture of solution A and solution B (at a ratio of 1:1) for two weeks at room temperature in the dark. Then they were transferred to solution C for five days in the same environment, and solution C was renewed during the first 24 h. Afterward, coronal slices with a thickness of 100 μm were prepared using a Leica cryostat microtome (Leica CM1950). The slices were further stained according to the

manufacturer's instructions and then imaged using a 63 × /1.3 NA oil objective on an Olympus FV1200 confocal microscope (Olympus, Japan). The dendritic spine density of neurons in the CA1 region was analyzed using Image J software.

4.16. H&E staining

The mice's major organs (heart, liver, spleen, lung, kidney) were stained with H&E to investigate the biocompatibility of the CSPA NPs. All the above staining procedures were carried out by Servicebio Biotechnology Co., Ltd., Wuhan.

4.17. Copper salt staining

The deposition of CSPA NPs in the hippocampus was identified by copper staining with a kit (Abcam, Cambridge, Massachusetts, USA). Briefly, the working rhodamine solution was prepared by mixing 4 mL of rhodamine stock solution with 46 mL of acetate buffer solution. The brain sections were deparaffinized hydrated in distilled water and placed in a warm working solution. Subsequently, the solution was carefully stirred and allowed to cool to room temperature for 15–20 min. The sections were rinsed twice with acetate buffer solution for 1 min each time, dipped five times in hematoxylin solution, and rinsed three times with acetate buffer solution. Then the sections were dehydrated in absolute alcohol three times for 1 min each time and cleared in xylene before fixation. Finally, the sections were imaged with an Olympus microscope for the detection of copper deposits.

4.18. Treatment of animals with CSPA NPs

On PND 28, the mice were divided into five groups: healthy mice (control group), and sevoflurane-treated mice, which were 2) received PBS (Sev + PBS group); 3) received PBS after sonication with focused ultrasound (Sev + PBS + US group); 4) received CSPA@CM NPs (Sev + CSPA@CM group); and 5) received CSPA@CM NPs after sonication with focused ultrasound (Sev + CSPA@CM + US group). PBS and CSPA@CM were administered intravenously.

To better deliver CSPA@CM NPs to the hippocampus, ultrasound was used to transiently open the BBB. Before sonication, 50 μL of microbubbles (with a mean diameter of approximately 2 μm and a concentration of about 1×10^9 bubbles/mL) were intravenously injected into the mice on PNDs 28 and 30. The focus point of the ultrasonic probe was above the dorsolateral hippocampus according to the mouse brain map. The parameters used were 0.5 MHz frequency, 0.6 MPa acoustic pressure, 1 ms pulse interval, and 90 s sonication time. A total of 5 mg/kg of CSPA@CM NPs were injected intravenously into sevoflurane-treated mice on PNDs 28 and 30.

4.19. Morris water maze (MWM) test

On PNDs 31–36, the memory and cognitive abilities of the mice were tested using the MWM test. Briefly, the maze was composed of a round pool (150 cm in diameter and 80 cm in height, divided into four quadrants), and a movable platform (6 cm in diameter) in the middle of one quadrant. The pool was filled with water opacified with titanium dioxide (35 °C), and the water was 1.5 cm above the top of the movable platform. The MWM test consisted of a place navigation test on PNDs 31–35 and a spatial probe test on PND 36. On the phase of place navigation test, each mouse was trained four times per day with an interval of 60 min of rest after each test. At the beginning of each test, the mice were placed in the water facing the wall and searched for the hidden platform for 60 s. When the mice reached the hidden platform, they were allowed to stay for 15 s. If the mice failed, they were guided to find the platform and stayed for 15 s to strengthen their memories. On PND 36, the hidden platform was removed and the mice were placed in the quadrant opposite to the platform and swam freely for 60 s. A video tracking system (XR-XM101, Shanghai Xinruan Information Technology Co., Ltd) was used to record the movements of the mice in the pool, including the number of crossing times, the time spent in the target quadrant, and the swimming speed for further analysis. When all mice were examined by the MWM test, they were sacrificed, and tissues were collected for further experiments.

4.20. Open field test

The open field test (OFT) was performed to assess the anxiety and depression in the mice. The size of the OF arena was 50 × 50 × 40 cm. The arena was cleaned thoroughly with a 5 % alcohol/water solution between each test to minimize odor cues. Each mouse was placed in one designated corner to record its behavior for 10 min and then assessed by a SuperMaze Morris Video analysis system (XR-XZ301, Shanghai Xinruan Information Technology Co., Ltd). The distance traveled, average speed, time spent in the center arena, and time spent in the center of the arena were calculated and analyzed.

4.21. Novel object recognition test

The novel object recognition (NOR) test was used to assess learning and memory of mice as previously described [10]. During the habituation session, the mice were placed in the arena to explore for 10 min. After habituation, two objects of similar size but different shapes and colors were placed in the corners of the arena (5 cm away from the wall). Then, the mice were placed in the arena and allowed to freely explore for 10 min. Twenty-four hours later, one object was replaced, and the same test mice were allowed to explore. The exploration time of the mice was recorded and analyzed with XR-XZ301 (Shanghai Xinruan Information Technology Co., Ltd). The discrimination index was calculated as follows: Discrimination index = (% time with novel object)/(% time with novel object + % time with familiar object).

4.22. Acute brain slice electrophysiology

Mice were anesthetized to prepare transverse hippocampal slices (400 μm) by standard methods, at a temperature of 33 °C. One hour later, these brain slices were transported to the recording chamber and perfused with ACSF (mM): NaCl, 124; KCl, 2.5; NaH_2PO_4, 1.2; $NaHCO_3$, 24; HEPES, 5; glucose, 12.5; $MgSO_4$, 2; and $CaCl_2$, 2. The whole-cell patch-clamp recordings of CA1 pyramidal neurons were visualized by using infrared differential interference contrast (IR-DIC) video microscopy with a 40 × magnification water-immersion objective (BX51WI, Olympus, Japan). Spontaneous excitatory postsynaptic currents (sEPSCs) were recorded by a Multiclamp 700B amplifier (Molecular Devices). Pipette resistance was 3–8 MΩ. The internal solution contained (in mM): K-gluconate, 120; HEPES, 10; $MgCl_2$, 1; $CaCl_2$, 1; KCl, 11; EGTA,11; MgATP, 4; and NaGTP, 0.5; pH 7.2, osmolarity 290 mOsm. Membrane potential responses under current-clamp conditions were sampled at 50 kHz and filtered at 10 kHz and bridge balance values > 20 MΩ were discarded. Under voltage clamp conditions, data acquisition was sampled at 20 kHz and filtered at 10 kHz. Cells were held at a membrane potential of −70 mV to evaluate sEPSCs. Recordings with a series resistance greater than 20 MΩ were discarded, and series resistance was compensated to 70 %. Analysis of electrophysiological data was performed using Clampfit (v10.3; Molecular Devices).

5. Statistics

Statistical tests were performed using GraphPad Prism 9 (GraphPad Software, La Jolla, CA). The data were presented as the mean ± SEM. The normality of the data was tested with the Shapiro-Wilk normality test. Student's t-test was performed for comparisons between the two groups. One-way analysis of variance (ANOVA) or two-way ANOVA with Tukey's post hoc test was performed for multiple comparisons. For

all experiments, statistical significance was defined as follows: not significant (n.s.), $^{*}P < 0.05$, $^{**}P < 0.01$, and $^{***}P < 0.001$.

CRediT authorship contribution statement

Gang Wang: Writing – original draft, Validation, Project administration, Methodology, Investigation. **Yaobao Han:** Writing – original draft, Project administration, Formal analysis, Data curation. **Ke Peng:** Project administration, Formal analysis. **Zhilin Jiang:** Project administration, Formal analysis, Data curation. **Tingting Wang:** Project administration, Formal analysis, Data curation. **Qing Zheng:** Writing – original draft. **Wenting Li:** Formal analysis. **Hanbing Xu:** Formal analysis. **Fuhai Ji:** Writing – review & editing, Supervision, Funding acquisition, Data curation, Conceptualization. **Zhen Li:** Supervision, Investigation, Funding acquisition, Formal analysis, Conceptualization.

Declaration of competing interest

The authors declare no conflict of interest.

Acknowledgments

The authors acknowledge the support from the National Key Research and Development Program of China (2022YFA1104300), the Interdisciplinary Basic Frontier Innovation Program of Suzhou Medical College of Soochow University (YXY2303025), the Major Basic Research Project of the Natural Science Foundation of the Jiangsu Higher Education Institutions (22KJA310004), the Key Medical Research Projects in Jiangsu Province (grant number: ZD2022021), the Suzhou Medical Health Science and Technology Innovation Project (SKY2022136), National Natural Science Foundationof China (82471281) and the National Clinical Key Specialty for Anesthesiology (First Affiliated Hospital of Soochow University). The authors also are grateful for support from the Jiangsu Provincial Key Laboratory of Radiation Medicine and Protection, the Priority Academic Program Development of Jiangsu Higher Education Institutions (PAPD).

Appendix A. Supplementary data

Supplementary data to this article can be found online at https://doi.org/10.1016/j.mtbio.2025.101714.

Data availability

Data will be made available on request.

References

[1] D. Hu, R.P. Flick, M.J. Zaccariello, et al., Association between exposure of young children to procedures requiring general anesthesia and learning and behavioral outcomes in a population-based birth cohort, Anesthesiology 127 (2017) 227–240, https://doi.org/10.1097/aln.0000000000001735.

[2] R.T. Wilder, R.P. Flick, J. Sprung, et al., Early exposure to anesthesia and learning disabilities in a population-based birth cohort, Anesthesiology 110 (2009) 796–804, https://doi.org/10.1097/01.anes.0000344728.34332.5d.

[3] C. Ing, C. DiMaggio, A. Whitehouse, et al., Long-term differences in language and cognitive function after childhood exposure to anesthesia, Pediatrics 130 (2012) e476–e485, https://doi.org/10.1542/peds.2011-3822.

[4] T.G. Hansen, J.K. Pedersen, S.W. Henneberg, et al., Academic performance in adolescence after inguinal hernia repair in infancy: a nationwide cohort study, Anesthesiology 114 (2011) 1076–1085, https://doi.org/10.1097/ALN.0b013e31820e77a0.

[5] G.J. Walkden, H. Gill, N.M. Davies, et al., Early childhood general anesthesia and neurodevelopmental outcomes in the avon longitudinal study of parents and children birth cohort, Anesthesiology 133 (2020) 1007–1020, https://doi.org/10.1097/aln.0000000000003522.

[6] C.H. Ing, C.J. DiMaggio, E. Malacova, et al., Comparative analysis of outcome measures used in examining neurodevelopmental effects of early childhood anesthesia exposure, Anesthesiology 120 (2014) 1319–1332, https://doi.org/10.1097/aln.0000000000000248.

[7] X. Xu, C. Li, J. Zou, et al., MiR-34a targets SIRT1 to reduce p53 deacetylation and promote sevoflurane inhalation anesthesia-induced neuronal autophagy and apoptosis in neonatal mice, Exp. Neurol. 368 (2023) 114482, https://doi.org/10.1016/j.expneurol.2023.114482.

[8] N. Useinovic, S. Maksimovic, C. Liechty, et al., Systemic inflammation exacerbates developmental neurotoxicity induced by sevoflurane in neonatal rats, Br. J. Anaesth. 129 (2022) 555–566, https://doi.org/10.1016/j.bja.2022.05.008.

[9] T. Fehr, W.G.M. Janssen, J. Park, et al., Neonatal exposures to sevoflurane in rhesus monkeys alter synaptic ultrastructure in later life, iScience 25 (2022) 105685, https://doi.org/10.1016/j.isci.2022.105685.

[10] W. Li, X. Meng, K. Peng, et al., Boosting microglial lipid metabolism via TREM2 signaling by biomimetic nanoparticles to attenuate the sevoflurane-induced developmental neurotoxicity, Adv. Sci. (2023) e2305989, https://doi.org/10.1002/advs.202305989.

[11] B. Chen, Y. Liu, Y. Cai, et al., Hippocampus is more vulnerable to neural damages induced by repeated sevoflurane exposure in the second trimester than other brain areas, Acta Biochim. Biophys. Sin. 52 (2020) 864–874, https://doi.org/10.1093/abbs/gmaa060.

[12] Y. Wu, Z. Yang, S. Su, et al., Differential epitranscriptome and proteome modulation in the brain of neonatal mice exposed to isoflurane or sevoflurane, Cell Biol. Toxicol. 39 (2023) 2133–2148, https://doi.org/10.1007/s10565-022-09701-9.

[13] L.L. Qiu, X.X. Tan, J.J. Yang, et al., Lactate improves long-term cognitive impairment induced by repeated neonatal sevoflurane exposures through SIRT1-mediated regulation of adult hippocampal neurogenesis and synaptic plasticity in male mice, Mol. Neurobiol. 60 (2023) 5273–5291, https://doi.org/10.1007/s12035-023-03413-9.

[14] S. Khodaei, D.S. Wang, Y. Lee, et al., Sevoflurane and lipopolysaccharide-induced inflammation differentially affect γ-aminobutyric acid type A receptor-mediated tonic inhibition in the hippocampus of male mice, Br. J. Anaesth. 130 (2023) e7–e10, https://doi.org/10.1016/j.bja.2022.09.013.

[15] C. Cangalaya, S. Wegmann, W. Sun, et al., Real-time mechanisms of exacerbated synaptic remodeling by microglia in acute models of systemic inflammation and tauopathy, Brain Behav. Immun. 110 (2023) 245–259, https://doi.org/10.1016/j.bbi.2023.02.023.

[16] Y. Xu, G. Gao, X. Sun, et al., ATPase inhibitory factor 1 is critical for regulating sevoflurane-induced microglial inflammatory responses and caspase-3 activation, Front. Cell. Neurosci. 15 (2021) 770666, https://doi.org/10.3389/fncel.2021.770666.

[17] Q. Wu, Y. Zhou, J. Yan, et al., Biomimetic nanocomplexes orchestrate post-stroke cerebral microenvironment via microglia-targeted siRNA delivery, Nano Today 58 (2024) 102444, https://doi.org/10.1016/j.nantod.2024.102444.

[18] Z. Wu, Y. Zhang, Y. Zhang, et al., Sirtuin 2 inhibition attenuates sevoflurane-induced learning and memory deficits in developing rats via modulating microglial activation, Cell. Mol. Neurobiol. 40 (2020) 437–446, https://doi.org/10.1007/s10571-019-00746-9.

[19] Y. Dai, M. Yan, J. Wan, et al., Maf1 mitigates sevoflurane-induced microglial inflammatory damage and attenuates microglia-mediated neurotoxicity in HT-22 cells by activating the AMPK/Nrf2 signaling, Neurotoxicology 90 (2022) 237–245, https://doi.org/10.1016/j.neuro.2022.04.003.

[20] P. Izquierdo, H. Shiina, C. Hirunpattarasilp, et al., Synapse development is regulated by microglial THIK-1 K(+) channels, Proc. Natl. Acad. Sci. U. S. A. 118 (2021), https://doi.org/10.1073/pnas.2106294118.

[21] R.C. Paolicelli, G. Bolasco, F. Pagani, et al., Synaptic pruning by microglia is necessary for normal brain development, Science 333 (2011) 1456–1458, https://doi.org/10.1126/science.1202529.

[22] J. Spurrier, L. Nicholson, X.T. Fang, et al., Reversal of synapse loss in Alzheimer mouse models by targeting mGluR5 to prevent synaptic tagging by C1Q, Sci. Transl. Med. 14 (2022) eabi8593, https://doi.org/10.1126/scitranslmed.abi8593.

[23] D.K. Wilton, K. Mastro, M.D. Heller, et al., Microglia and complement mediate early corticostriatal synapse loss and cognitive dysfunction in Huntington's disease, Nat Med 29 (2023) 2866–2884, https://doi.org/10.1038/s41591-023-02566-3.

[24] N.D. Schartz, A.J. Tenner, The good, the bad, and the opportunities of the complement system in neurodegenerative disease, J. Neuroinflammation 17 (2020) 354, https://doi.org/10.1186/s12974-020-02024-8.

[25] Q. Cong, B.M. Soteros, A. Huo, et al., C1q and SRPX2 regulate microglia mediated synapse elimination during early development in the visual thalamus but not the visual cortex, Glia 70 (2022) 451–465, https://doi.org/10.1002/glia.24114.

[26] B. Stevens, N.J. Allen, L.E. Vazquez, et al., The classical complement cascade mediates CNS synapse elimination, Cell 131 (2007) 1164–1178, https://doi.org/10.1016/j.cell.2007.10.036.

[27] S. Werneburg, J. Jung, R.B. Kunjamma, et al., Targeted complement inhibition at synapses prevents microglial synaptic engulfment and synapse loss in demyelinating disease, Immunity 52 (2020) 167–182.e167, https://doi.org/10.1016/j.immuni.2019.12.004.

[28] H. Yang, C.K. Oh, H. Amal, et al., Mechanistic insight into female predominance in Alzheimer's disease based on aberrant protein S-nitrosylation of C3, Sci. Adv. 8 (2022) eade0764, https://doi.org/10.1126/sciadv.ade0764.

[29] H. Lui, J. Zhang, S.R. Makinson, et al., Progranulin deficiency promotes circuit-specific synaptic pruning by microglia via complement activation, Cell 165 (2016) 921–935, https://doi.org/10.1016/j.cell.2016.04.001.

[30] B. Dejanovic, M.A. Huntley, A. De Mazière, et al., Changes in the synaptic proteome in tauopathy and rescue of tau-induced synapse loss by C1q antibodies, Neuron 100 (2018) 1322–1336.e1327, https://doi.org/10.1016/j.neuron.2018.10.014.

[31] M. Mohebnasab, O. Eriksson, B. Persson, et al., Current and future approaches for monitoring responses to anti-complement therapeutics, Front. Immunol. 10 (2019) 2539, https://doi.org/10.3389/fimmu.2019.02539.
[32] W.M. Zelek, L. Xie, B.P. Morgan, et al., Compendium of current complement therapeutics, Mol. Immunol. 114 (2019) 341–352, https://doi.org/10.1016/j.molimm.2019.07.030.
[33] M.C. Dalakas, H. Alexopoulos, P.J. Spaeth, Complement in neurological disorders and emerging complement-targeted therapeutics, Nat. Rev. Neurol. 16 (2020) 601–617, https://doi.org/10.1038/s41582-020-0400-0.
[34] H. Liu, Y. Han, T. Wang, et al., Targeting microglia for therapy of Parkinson's disease by using biomimetic ultrasmall nanoparticles, J. Am. Chem. Soc. 142 (2020) 21730–21742, https://doi.org/10.1021/jacs.0c09390.
[35] H. Zhang, T. Wang, W. Qiu, et al., Monitoring the opening and recovery of the blood-brain barrier with noninvasive molecular imaging by biodegradable ultrasmall Cu(2- x)Se nanoparticles, Nano Lett. 18 (2018) 4985–4992, https://doi.org/10.1021/acs.nanolett.8b01818.
[36] P. Zhao, J. Qu, A. Wu, et al., Anti-alcoholism drug disulfiram for targeting glioma energy metabolism using BBB-penetrating delivery of fixed-dose combination, Nano Today 44 (2022) 101448, https://doi.org/10.1016/j.nantod.2022.101448.
[37] J. Yuan, H. Liu, H. Zhang, et al., Controlled activation of TRPV1 channels on microglia to boost their autophagy for clearance of alpha-synuclein and enhance therapy of Parkinson's disease, Adv Mater 34 (2022) e2108435, https://doi.org/10.1002/adma.202108435.
[38] Q. Zheng, H. Liu, H. Zhang, et al., Ameliorating mitochondrial dysfunction of neurons by biomimetic targeting nanoparticles mediated mitochondrial biogenesis to boost the therapy of Parkinson's disease, Adv. Sci. 10 (2023) e2300758, https://doi.org/10.1002/advs.202300758.
[39] H. Liu, Q. Zheng, J. Yuan, et al., Modulating SQSTM1/p62-dependent selective autophagy of neurons by activating Nrf2 with multifunctional nanoparticles to eliminate α-synuclein aggregates and boost therapy of Parkinson's disease, Nano Today 49 (2023) 101770, https://doi.org/10.1016/j.nantod.2023.101770.
[40] D.P. Schafer, E.K. Lehrman, A.G. Kautzman, et al., Microglia sculpt postnatal neural circuits in an activity and complement-dependent manner, Neuron 74 (2012) 691–705, https://doi.org/10.1016/j.neuron.2012.03.026.
[41] S.G. Torres-Platas, S. Comeau, A. Rachalski, et al., Morphometric characterization of microglial phenotypes in human cerebral cortex, J. Neuroinflammation 11 (2014) 12, https://doi.org/10.1186/1742-2094-11-12.
[42] H.Y. Chung, J. Wickel, N. Hahn, et al., Microglia mediate neurocognitive deficits by eliminating C1q-tagged synapses in sepsis-associated encephalopathy, Sci. Adv. 9 (2023) eabq7806, https://doi.org/10.1126/sciadv.abq7806.
[43] J. Bourel, V. Planche, N. Dubourdieu, et al., Complement C3 mediates early hippocampal neurodegeneration and memory impairment in experimental multiple sclerosis, Neurobiol. Dis. 160 (2021) 105533, https://doi.org/10.1016/j.nbd.2021.105533.
[44] C. Wang, H. Yue, Z. Hu, et al., Microglia mediate forgetting via complement-dependent synaptic elimination, Science 367 (2020) 688–694, https://doi.org/10.1126/science.aaz2288.
[45] Y. Qin, Q. Wen, J. Cao, et al., Flavonol glycosides and other phenolic compounds from Viola tianshanica and their anti-complement activities, Pharm. Biol. 54 (2016) 1140–1147, https://doi.org/10.3109/13880209.2015.1055635.
[46] E.H. Kim, Y.Y. Shim, H.I. Lee, et al., Astragalin and isoquercitrin isolated from aster scaber suppress LPS-induced neuroinflammatory responses in microglia and mice, Foods 11 (2022), https://doi.org/10.3390/foods11101505.
[47] G. Yao, Z. Bai, J. Niu, et al., Astragalin attenuates depression-like behaviors and memory deficits and promotes M2 microglia polarization by regulating IL-4R/JAK1/STAT6 signaling pathway in a murine model of perimenopausal depression, Psychopharmacology (Berl) 239 (2022) 2421–2443, https://doi.org/10.1007/s00213-022-06133-5.
[48] M.J. Vasek, S.M. Mueller, S.B. Fass, et al., Local translation in microglial processes is required for efficient phagocytosis, Nat. Neurosci. 26 (2023) 1185–1195, https://doi.org/10.1038/s41593-023-01353-0.
[49] S. Song, L. Yu, M.N. Hasan, et al., Elevated microglial oxidative phosphorylation and phagocytosis stimulate post-stroke brain remodeling and cognitive function recovery in mice, Commun. Biol. 5 (2022) 35, https://doi.org/10.1038/s42003-021-02984-4.
[50] J.D. Quick, C. Silva, J.H. Wong, et al., Lysosomal acidification dysfunction in microglia: an emerging pathogenic mechanism of neuroinflammation and neurodegeneration, J. Neuroinflammation 20 (2023) 185, https://doi.org/10.1186/s12974-023-02866-y.
[51] H. Iyer, K. Shen, A.M. Meireles, et al., A lysosomal regulatory circuit essential for the development and function of microglia, Sci. Adv. 8 (2022) eabp8321, https://doi.org/10.1126/sciadv.abp8321.
[52] S. Yang, Y. Cheng, M. Liu, et al., Sequential assembly of DNA nanoparticles inside cells enables lysosome interference and cell behavior regulation, Nano Today 56 (2024) 102224, https://doi.org/10.1016/j.nantod.2024.102224.
[53] A.W. Kao, A. McKay, P.P. Singh, et al., Progranulin, lysosomal regulation and neurodegenerative disease, Nat. Rev. Neurosci. 18 (2017) 325–333, https://doi.org/10.1038/nrn.2017.36.
[54] Y. Tanaka, T. Matsuwaki, K. Yamanouchi, et al., Increased lysosomal biogenesis in activated microglia and exacerbated neuronal damage after traumatic brain injury in progranulin-deficient mice, Neuroscience 250 (2013) 8–19, https://doi.org/10.1016/j.neuroscience.2013.06.049.
[55] Z. Guan, Z. Chen, S. Fu, et al., Progranulin administration attenuates β-amyloid deposition in the Hippocampus of 5xFAD mice through modulating BACE1 expression and microglial phagocytosis, Front. Cell. Neurosci. 14 (2020) 260, https://doi.org/10.3389/fncel.2020.00260.
[56] D.H. Paushter, H. Du, T. Feng, et al., The lysosomal function of progranulin, a guardian against neurodegeneration, Acta Neuropathol. 136 (2018) 1–17, https://doi.org/10.1007/s00401-018-1861-8.
[57] C. Yang, X. Wang, Lysosome biogenesis: regulation and functions, J. Cell Biol. 220 (2021), https://doi.org/10.1083/jcb.202102001.
[58] C. Settembre, C. Di Malta, V.A. Polito, et al., TFEB links autophagy to lysosomal biogenesis, Science 332 (2011) 1429–1433, https://doi.org/10.1126/science.1204592.
[59] Y. Tanaka, J.K. Chambers, T. Matsuwaki, et al., Possible involvement of lysosomal dysfunction in pathological changes of the brain in aged progranulin-deficient mice, Acta Neuropathol Commun 2 (2014) 78, https://doi.org/10.1186/s40478-014-0078-x.
[60] F. Hu, T. Padukkavidana, C.B. Vægter, et al., Sortilin-mediated endocytosis determines levels of the frontotemporal dementia protein, progranulin, Neuron 68 (2010) 654–667, https://doi.org/10.1016/j.neuron.2010.09.034.
[61] J.V. Pluvinage, M.S. Haney, B.A.H. Smith, et al., CD22 blockade restores homeostatic microglial phagocytosis in ageing brains, Nature 568 (2019) 187–192, https://doi.org/10.1038/s41586-019-1088-4.
[62] L. Lu, X. Liu, J. Fu, et al., sTREM-1 promotes the phagocytic function of microglia to induce hippocampus damage via the PI3K-AKT signaling pathway, Sci. Rep. 12 (2022) 7047, https://doi.org/10.1038/s41598-022-10973-8.
[63] J. Liu, L. Li, P. Xie, et al., Sevoflurane induced neurotoxicity in neonatal mice links to a GSK3β/Drp1-dependent mitochondrial fission and apoptosis, Free Radic. Biol. Med. 181 (2022) 72–81, https://doi.org/10.1016/j.freeradbiomed.2022.01.031.
[64] D.P. Schafer, E.K. Lehrman, C.T. Heller, et al., An engulfment assay: a protocol to assess interactions between CNS phagocytes and neurons, J. Vis. Exp. (2014), https://doi.org/10.3791/51482.
[65] G Wang, HY Liu, XW Meng, et al., Complement C1q-mediated microglial synaptic elimination by enhancing desialylation underlies sevoflurane-induced developmental neurotoxicity, Cell Biosci 14 (1) (2024) 42, https://doi.org/10.1186/s13578-024-01223-7.